Research Article | Vol. 30, No. 22 / 24 Oct 2022 / Optics Express 39946
Optics EXPRESS

Fabry–Perot interferometers for highly-sensitive multi-point relative humidity sensing based on Vernier effect and digital signal processing

YU WANG,[1] YAXI YAN,[2,*] ZHENGGANG LIAN,[3] DARU CHEN,[2] ALAN PAK TAO LAU,[4] AND CHAO LU[1]

[1]*Photonics Research Institute, Department of Electronic and Information Engineering, Hong Kong Polytechnic University, Hong Kong, China*
[2]*Hangzhou Institute of Advanced Studies, Zhejiang Normal University, Hangzhou, China*
[3]*Yangtze Optical Electronics Co., Ltd. (YOEC), Fifth Hi-Tech Avenue, East Lake Hi-Tech Develop Zone, Wuhan, China*
[4]*Photonics Research Institute, Department of Electrical Engineering, Hong Kong Polytechnic University, Hong Kong, China*
[*]*ya.xi.yan@connect.polyu.hk*

Abstract: A highly sensitive relative humidity (RH) sensor based on Fabry-Perot interferometers (FPI) is proposed and experimentally demonstrated. The sensor is fabricated by splicing a segment of hollow core Bragg fiber (HCBF) with single mode fiber (SMF) and functionalized with chitosan and ultraviolet optical adhesive (UVOA) composite at the end of HCBF to form a hygroscopic polymer film. The reflection beams from the splicing point and the two surfaces of the polymer film generate the Vernier effect in the reflection spectrum, which significantly improves the humidity sensitivity of the sensor. To demodulate the envelope based on the Vernier effect and realize multi-point sensing, a digital signal processing (DSP) algorithm is proposed to process the reflection spectrum. The performance of the DSP algorithm is theoretically analyzed and experimentally verified. The proposed sensor demonstrates a high sensitivity of 1.45 nm/% RH for RH ranging from 45% RH to 90% RH. The compact size, high sensitivity and multiplexing capability make this sensor a promising candidate for RH monitoring. Furthermore, the proposed DSP can potentially be applied to other sensors based on the Vernier effect to analyze and extract valuable information from the interference spectrum.

1. Introduction

Relative humidity (RH) measurements and control are of great importance in various industrial fields, such as production and storage of food and computer components, environmental monitoring, chemical synthesis, and civil engineering [1–4]. Numerous humidity sensors were proposed for precise humidity monitoring in the past decade [5–7]. Conventional electronic RH sensors achieve RH detection based on variation of capacitance, resistance, and conductivity of electronic components on humidity [8,9]. However, the intrinsic properties of electronic devices hinder their applications in remote monitoring and usability in narrow space and electromagnetic-interference conditions [10]. Recently, optical fiber sensors have attracted considerable attention thanks to their unique advantages compared with their electronic counterparts, such as compact size, light weight, high stability, and electromagnetic immunity [11,12]. Meanwhile, the optical signal can transmit in fiber with low loss, enabling multi-point and remote sensing [13,14]. It can also be used for RH monitoring in hazardous environments such as downhole and chemical synthesis workshops. However, silica is intrinsically insensitive to humidity. This leads to the low sensitivity of all-silica fiber RH sensors [10]. Therefore, typical fiber sensing schemes are commonly integrated with hygroscopic materials, such as PVA (Poly(vinyl alcohol)) [15],

#470755 https://doi.org/10.1364/OE.470755
Journal © 2022 Received 19 Jul 2022; revised 14 Sep 2022; accepted 26 Sep 2022; published 13 Oct 2022

Optics EXPRESS

agarose [16], and chitosan [17], which undergo a greater change in refractive index (RI) or volume under different humidity, to achieve higher sensitivity and better performance. Besides, to improve the interaction between the evanescent field and the hydrophilic materials, many micromachining techniques, such as tapering [18], etching [19] and femtosecond processing [20], have been applied to optical sensing fiber. Although effective, these processes typically rely on expensive equipment and the sensing structures are fragile, which hinders large-scale commercial production and practical utilization.

As a kind of sensor that does not rely heavily on the expensive precision instrument, the Fabry-Perot interferometer (FPI) has been widely used in fiber humidity sensing due to its characteristics of high integrality, miniaturization, and simple configuration [21,22]. Different FPI schemes have been reported, including thin films [23], hybrid cavities [24] and microtips [25]. For instance, in 2012, L. Chen et al. proposed a chitosan-based FP humidity sensor [17], where a diaphragm of hygroscopic material is bonded at the end of the hollow core fiber to form the reflector of FPI. The RH variations would cause the diaphragm's elastic deformation, leading to the change in the FPI cavity length. Similar structures relying on plentiful types of microcavities and thin films have been proposed consecutively [26]. These FPIs are commonly formed by dipping, spin coating, hydroxide catalysis bonding or 3D femtosecond machining. It is noted that the shorter the cavity length, the higher the sensitivity. However, it is not easy to form an extremely short FP cavity while maintaining the uniformity of the thin film.

Therefore, the Vernier effect has been introduced to FPI-based sensors to improve the sensitivity under current microcavity processing technology [27]. In the Vernier effect, two interferometers with small free spectral range (FSR) difference are used to create a superimposed spectrum. By monitoring the response of the extracted envelope, the sensor's sensitivity is amplified by orders of magnitude. The sensitization mechanism has been successfully integrated with FPI, Mach-Zehnder interferometer (MZI), and Sagnac interferometer to detect temperature, curvature, strain, gas pressure, etc. [28,29]. Various works based on the Vernier effect combined with FPI for humidity sensing have been demonstrated [15,30]. In these works, the widely used method to extract the spectra envelope formed by the Vernier effect is to connect the peaks of high-frequency fringes. However, the results obtained by this method are imprecise, and such a method is invalid when the spectrum is influenced by noises that make the envelope unrecognized. In addition, when multiple sensing heads are integrated, the superimposed spectra are too complex to distinguish the shifts of the envelope corresponding to each sensor. This simple fitting method results in the incapability of multi-point sensing. Thus, developing a novel method to effectively demodulate the spectra based on the Vernier effect is essential to achieving high-precision and multi-point humidity measurement.

In this paper, we present an extrinsic FPI for multi-point RH sensing based on a homemade hollow core Bragg fiber (HCBF) and the Vernier effect. The sensing probe is fabricated by splicing a section of HCBF with conventional single-mode fiber (SMF). A hygroscopic thin film composed of ultraviolet optical adhesive (UVOA) and chitosan is coated at the tip of the HCBF. Using our two-step film manufacture method, a thin film with two smooth surfaces and high reflectivities is fabricated, forming a triple-beam interferometer. Based on the Vernier effect, the interference fringes generate an envelope in the reflected spectrum, which can be used to realize highly sensitive RH sensing. The spectra are demodulated using a well-designed digital signal processing (DSP) approach based on fast Fourier transform (FFT), filtering, and inverse fast Fourier transform (IFFT). The method can extract the Vernier effect-based envelope accurately and conveniently. The algorithm's effectiveness is analyzed theoretically and verified experimentally by comparing the original spectra with the extracted envelopes. Our sensing structure based on the Vernier effect combined with the DSP algorithm can significantly improve the sensor's RH sensitivity to reach 1.45 nm/% RH. Meanwhile, three sensing probes with designed HCBF lengths are precisely fabricated under a microscope and connected in parallel

Optics EXPRESS

with a coupler to form a superimposed spectrum. Due to the different HCBF lengths of the sensors, the signals corresponding to them can be distinguished in the FFT spectrum, allowing our DSP algorithm to demodulate the Vernier effect envelopes for each sensor. This provides our sensing system with multi-point sensing capability. The entire fabrication process is simple without expensive equipment or chemical etching, which results in the low cost, satisfactory repeatability and safety of fabrication. More importantly, the proposed DSP algorithm is a promising method to demodulate other sensors based on multi-beam interference spectra.

2. Operating principle

2.1. Fabry-Perot interferometers based on Vernier effect

The configuration of our proposed RH sensor is shown in Fig. 1, which is formed by an SMF, a short section of HCBF and a thin polymer sensing diaphragm coated at the end face of HCBF. The HCBF has a concentric ring structure consisting of an air core surrounded by multiple high- and low-index silica layers. Light is guided in the core due to the anti-resonant reflecting optical waveguide (ARROW) effect [31]. The incident light transmitted along the lead-in SMF is partially reflected from the SMF-HCBF splicing point and the two surfaces of the polymer thin film. These three reflective mirrors are labeled as M_1, M_2 and M_3, respectively. These mirrors comprise an air FP cavity, a polymer FP cavity and an air-polymer hybrid cavity.

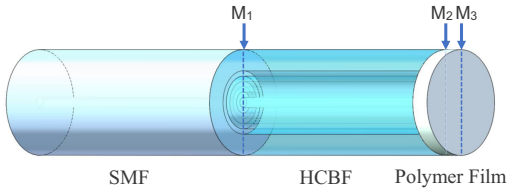

Fig. 1. The schematic diagram of our proposed RH sensor structure.

The RIs of air and the polymer film, labeled as n_1 and n_2, are approximately 1 and 1.45 in our experiment, respectively. According to Fresnel's reflection theory, the reflection coefficients at polymer-air interfaces are calculated as $[(n_2 - n_1)/(n_2 + n_1)]^2 = 3.37\%$, which are very low [17,32,33]. Therefore, the simplified method is only calculating the three beams that undergo one reflection reflected at the three mirrors. The light intensities attributed to multiple reflections are too weak and can be ignored. According to triple-beam interference theory, the reflected light can be written as [34]:

$$E_r = E_{in}[\sqrt{R_1} + Ae^{-j2\phi_1} + Be^{-j2(\phi_1+\phi_2)}], \tag{1}$$

where E_r and E_{in} are the incident and reflected electric field. $A = (1 - T_1)(1 - R_1)\sqrt{R_2}$ and $B = (1 - T_1)(1 - T_2)(1 - R_1)(1 - R_2)\sqrt{R_3}$. T_1 and T_2 are the transmission loss at air FP cavity and polymer FP cavity. R_i is the reflection coefficient of the mirror i ($i = 1, 2, 3$). $\phi_1 = 2\pi n_1 L/\lambda$ and $\phi_2 = 2\pi n_2 d/\lambda$ are the phase shifts in air cavity and polymer cavity, respectively. L and d refer to the lengths of such cavities. λ is the wavelength. Therefore, the light intensity reflected from the proposed cascaded FPIs can be expressed as:

$$\begin{aligned} I_r = (E_r)^2 = E_{in}^2 \Big[& R_1 + A^2 + B^2 + 2\sqrt{R_1}Acos(2\phi_1) \\ & +2ABcos(2\phi_2) + 2\sqrt{R_1}Bcos[2(\phi_1 + \phi_2)\Big]. \end{aligned} \tag{2}$$

Optics EXPRESS

By combining the two terms, i.e. $2\sqrt{R_1}Acos(2\phi_1)$ and $2\sqrt{R_1}Bcos[2(\phi_1+\phi_2)]$, Eq. (2) can be converted into the form as:

$$I_r = (E_r)^2 = E_{in}^2\left[R_1 + A^2 + B^2 + Esin(2\phi_1+\phi_2+\delta) + 2ABcos(2\phi_2)\right], \tag{3}$$

where E and δ are defined as:

$$E = 2\sqrt{R_1A^2 + R_1B^2 + 2R_1ABcos(2\phi_2)} \tag{4}$$

$$\delta = -arctan\left[A + Bcos(2\phi_1+\phi_2)/Bcos(\phi_2)\right]. \tag{5}$$

Equation (3) indicates that the high-frequency component determined by the term $sin(2\phi_1+\phi_2+\delta)$ will form dense interference fringes in the reflected spectra. The low-frequency component related to the term E has the same phase as the term $2ABcos(2\phi_2)$, which will modulate the interference fringes. Therefore, in the reflection spectrum, the high-frequency interference fringes will form an envelope with the same phase of $2\phi_2$.

When the external RH varies, the swelling and shrinking of the hygroscopic polymer layer will result in the variation of the film thickness d. At the same time, the RI n_2 changes accordingly. These will cause a change in phase ϕ_2 and finally lead to a shift in the envelope, which is a valuable indicator for RH monitoring.

For the traditional two-beam FPI-based sensor, the wavelength shift of the high-frequency fringe is commonly used to monitor the RH value [17]. For instance, in an interferometer formed by M1 and M3, when the cavity length of hybrid FP cavity $L + d$ changes with RH, the shift of the FPI fringe $\Delta\lambda_{FP}$ is conducted as:

$$\Delta\lambda_{FP} = \frac{\lambda}{Ln_1 + dn_2}\Delta(n_2d). \tag{6}$$

Similarly, the shift of the envelope $\Delta\lambda_{en}$ in our three-beam FPI is expressed as [30]:

$$\Delta\lambda_{en} = \frac{\lambda}{dn_2}\Delta(n_2d). \tag{7}$$

Therefore, the amplification factor based on the Vernier-effect envelope compared with traditional FPI is written as:

$$M = \frac{Ln_1 + dn_2}{dn_2}. \tag{8}$$

By making Ln_1 much larger than dn_2, the RH sensitivity would be improved significantly due to the Vernier effect.

2.2. Algorithms to demodulate the envelope

Equation (2) can be written in the form of optical frequency as

$$\begin{aligned} I_r = (E_r)^2 = E_{in}^2\Big[&R_1 + A^2 + B^2 + 2\sqrt{R_1}Acos(4\pi n_1Lf/c) \\ &+2ABcos(4\pi n_2df/c) + 2\sqrt{R_1}Bcos[4\pi(n_1L + n_2d)f/c\Big], \end{aligned} \tag{9}$$

where f and c are the frequency and velocity of light in vacuum, respectively. Here, the reflected spectrum is actually the summation of three cosine functions with different angular frequencies

Optics EXPRESS

[35–37]. By normalizing, the three cosine functions can be written as:

$$s_1 = cos(\omega_1 f), \tag{10}$$

$$s_2 = cos(\omega_2 f), \tag{11}$$

$$s_3 = cos(\omega_3 f), \tag{12}$$

where

$$\omega_1 = 4\pi n_1 L/c, \tag{13}$$

$$\omega_2 = 4\pi n_2 d/c, \tag{14}$$

$$\omega_3 = 4\pi(n_1 L + n_2 d)/c. \tag{15}$$

In our case, since d is much smaller than L, s_1 and s_3 are high frequency components with small frequency difference, while s_2 is a low frequency component.

We proposed a DSP method to extract the envelope from the superimposed spectrum. Figure 2 shows the detailed processing procedures, which contain several steps:

(i) Apply FFT to the raw reflected spectrum data. The original spectrum is mainly formed by two FP interferometers with similar cavity lengths, resulting in the obvious envelope related to the Vernier effect. After FFT, there are two dominant peaks in the spectrum, respectively marked in green and orange colors;

(ii) Use two band-pass filters to obtain the two high-frequency components s_1 (green color) and s_3 (orange color);

(iii) Multiply s_1 by s_3 and get a new component with the following form:

$$\begin{aligned} s_1 s_3 &= cos(4\pi n_1 L f/c) cos[4\pi(n_1 L + n_2 d)f/c] \\ &= 1/2\{cos[4\pi(2n_1 L + n_2 d)f/c] + cos(4\pi n_2 df/c)\}. \end{aligned} \tag{16}$$

Equation (16) indicates that the component $s_1 s_3$ contains one high frequency component $cos[4\pi(2n_1 L + n_2 d)f/c]$ and one low frequency component $cos(4\pi n_2 df/c)$.

(iv) Apply FFT to $s_1 s_3$. The high frequency component and the low frequency component of $s_1 s_3$ can be obviously observed in the spectrum (purple color). Then a low-pass filter is applied to obtain the low frequency component $cos(4\pi n_2 df/c)$, i.e. $cos(2\phi_2)$, and IFFT is conducted to the filtered result to achieve the envelope.

The phase of the curve is determined by $cos(2\phi_2)$. According to Eq. (3) and previous discussion, the phase of Vernier-effect related envelope is also the same as $cos(2\phi_2)$. Therefore, the wavelengths of the dips in the IFFT curve and the original spectrum envelope are consistent with each other. In conclusion, the curve obtained using our DSP method can be regarded as an effectively extracted envelope formed by the Vernier effect and can be used for sensing experiments. Note that the wavelength spectrum in Fig. 2 (blue color) is ideal. In practical measurement, the unevenness of the film interfaces and the deformation of the HCBF will decrease the visibility of the envelope. Therefore, the widely used method of connecting the fringe peaks to extract the spectra envelope is unavailable and inaccurate. However, our DSP algorithm can eliminate the low-frequency noise in the FFT spectrum and extract the desired signals, significantly improving the sensor's usability. In addition, by designing sensors with different HCBF lengths, the peaks corresponding to each sensing head in the FFT spectrum can be distinguished. When these sensors are connected parallel with couplers, the reflected superimposed spectrum is too complex to find available information (see dark blue curve in Fig. 2). However, using our FFT and filtering processes, peaks corresponding to each sensor can be extracted independently. This means that our structure combined with DSP algorithms can achieve multi-point simultaneous sensing.

Optics EXPRESS

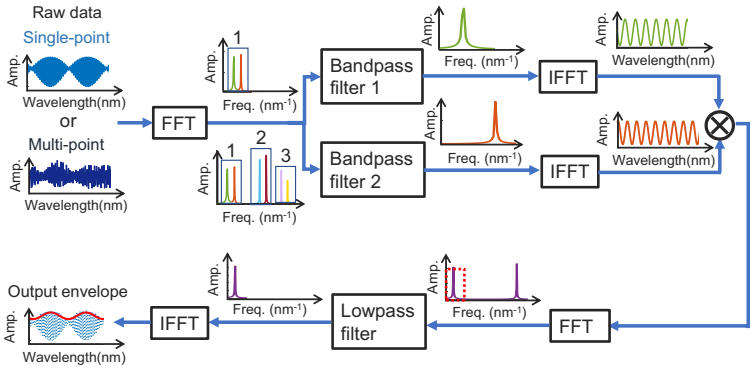

Fig. 2. The flowchart of DSP method.

3. Experiment and discussion

3.1. Sensor fabrication

The schematic diagrams of the fabrication processes of the proposed sensing structure are shown in Fig. 3. Firstly, a section of HCBF was spliced with a lead-in SMF (SMF-28 Corning) using a commercial fiber splicer (Fujikura 80S). The homemade HCBF was fabricated in our lab. The preform of the HCBF was fabricated by using the modified chemical vapor deposition (MCVD) equipment and drawn into the desired size via a modified drawing tower. The detail of the drawing process can be found in our previous work [11]. The scanning electron microscope (SEM) image of the HCBF cross-section is shown in Fig. 4(b). To improve the reflectivity, the parameters of fiber splicing were carefully optimized to avoid the deformation and collapse of the HCBF. Then, the HCBF was precisely cleaved under an optical microscope to achieve an expected length. After that, the tip of the HCBF was dipped vertically into a chitosan solution for 0.5 seconds. The concentration of the chitosan solution was chosen as 1% [17,30], prepared by mixing 1 *wt*% chitosan powder in acetic acid solution followed by magnetically stirring for 24 hours at room temperature. The probe was placed in a drying chamber with optimized humidity and temperature for 10 minutes to form a thin chitosan diaphragm at the end of the HCBF. Subsequently, another SMF with a thin droplet of UVOA (NOA61, Norland Products Inc) at the end face was aligned with the HCBF. The UVOA was then transferred to the HCBF by tip touching process and mixed with the chitosan. Here, the amount of UVOA can be adjusted by spin coating [38]. Finally, the UVOA was well cured under ultraviolet light for 1 hour to form the hybrid FP cavity. The schematic of the proposed sensor structure is shown in Fig. 4(a).

During the whole fabrication process, the reflected spectra were monitored in real-time. The sample with the HCBF length of 650 μm is set as an example to demonstrate the validity of our proposed DSP method. The interference spectra formed based on pure chitosan film and chitosan/UVOA composite film are shown in Fig. 5(a) and Fig. 5(b), respectively. The envelopes obtained by connecting the extreme points of the interference fringes are shown as the red lines. It is obvious that the visibility of the envelope improves significantly after introducing the UVOA. FFT is applied to the two reflected spectra, and the results are illustrated in Fig. 5(c). There is only one dominant peak in the FFT spectrum related to pure chitosan film (the green line), which means only two high reflectivity surfaces exist and form a double-beam interferometer. However, there are two peaks in the FFT spectrum of chitosan/UVOA hybrid membrane (the orange line). One of the peaks locates at the same abscissa position as the peak in the chitosan FFT spectrum, and the other is to the right of it. By analyzing the two FFT spectra, it can be concluded that the reflectivity of M_3 is much lower than that of M_2 for the pure chitosan film. It results in the

Optics EXPRESS

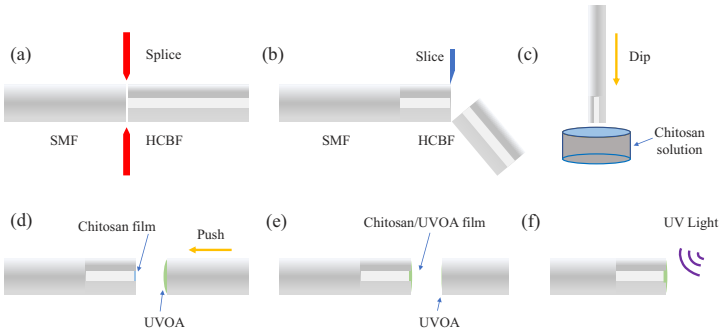

Fig. 3. The schematic diagrams of the fabrication processes of our proposed RH sensor. (a) Splice HCBF with SMF pigtail; (b) slice the HCBF to achieve an expected length; (c) dip the HCBF tip in chitosan solution; (d), (e) transform the UVOA to chitosan film by tip touching process; (f) cure the UVOA under ultraviolet light.

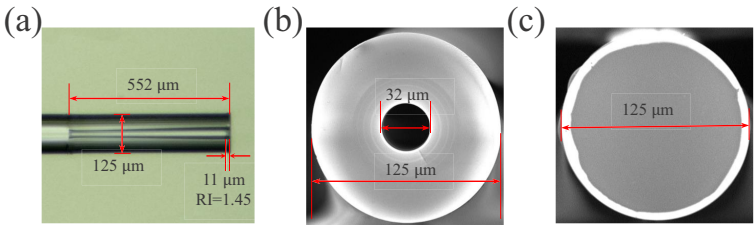

Fig. 4. (a) The microscope image of the fabricated sensing probe; (b) SEM images of the proposed HCBF before and (c) after coating with chitosan and UVOA.

indistinctness of the envelope shown in Fig. 5(a). When UVOA is coated at the end-face of HCBF and mixed with chitosan to form a new polymer diaphragm, the high reflectivity of M_2 remains while the surface M_3 is reshaped to be smoother. The cross-section SEM of the proposed sensor after coating with chitosan/UVOA is shown in Fig. 4(c). Two bandpass filters were applied to extract the two dominant frequency components and achieve the Vernier effect envelope formed by the two FPIs (see Fig. 5(b) (black line)). The black curve's dip wavelengths match well with those of the envelope extracted from the orange curve. It means our DSP method can figure out the Vernier effect-related envelope effectively and accurately.

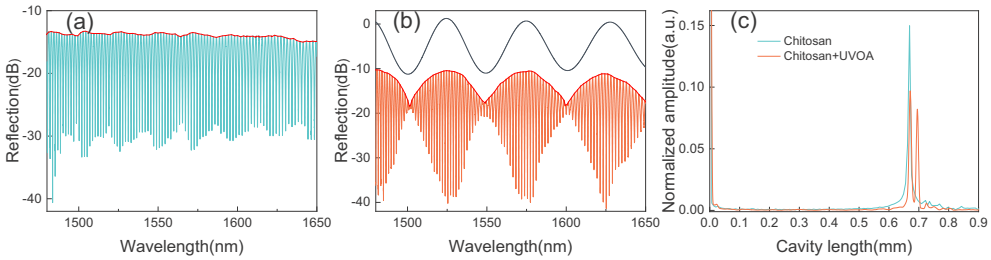

Fig. 5. (a) The reflected spectrum of the sensing probe coated with pure chitosan film. (b) The reflected spectrum of the sensing probe coated with chitosan/UVOA film (orange curve) and the extracted envelope by using our DSP method (black curve). (c) The fast Fourier Transform results of the reflected spectra.

Optics EXPRESS

3.2. Relative humidity response

The schematic diagram of the proposed humidity sensing system is shown in Fig. 6. The light launched from a broadband source (BBS) was transmitted along the SMF and reflected from the sensing head. The reflected signal passed through the optical circular and was recorded by the optical spectrum analyzer (OSA). The sensing head was mounted and fixed inside a commercial climate chamber, which can adjust the RH from 40% to 95% and temperature from 20 ° to 60 ° C. In the RH response test, the RH value in the chamber was increased from 45% to 90% with a step of 5% at a constant temperature of 27 °C. Before recording the reflected spectrum, the RH was stabilized for about 30 minutes after reaching the set value. The evolution of the reflected spectra in this process are shown in Fig. 7(a). The DSP was carried out, and the envelopes extracted from the reflected interference spectra are illustrated in Fig. 7(b). When the RH increases, the envelope exhibits a redshift. The dip around 1475 nm at 45% RH was chosen as the original tracing wavelength to analyze the RH sensitivity, as shown in Fig. 7(c). The sensor exhibits a good linear response in the RH sensing experiment. The RH sensitivity is calculated by using linear fitting as 1.42 nm/% RH.

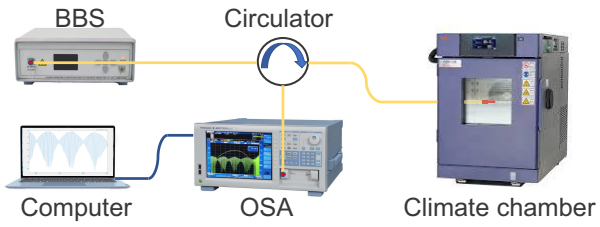

Fig. 6. The experimental setup of the humidity sensing system.

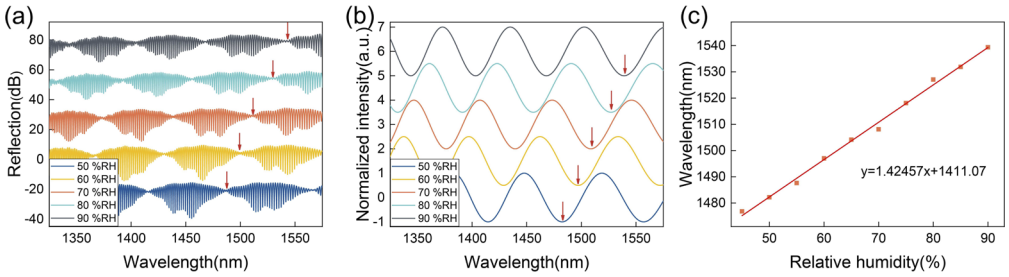

Fig. 7. (a) The reflected spectra evolution during the relative humidity response experiment. (b) Envelopes demodulated using the DSP method. (c) The wavelength at different RH and the relevant linear fitting result.

3.3. Temperature response

To investigate the temperature response of our proposed RH sensor, the ambient temperature was raised from 20 °C to 40 °C with an interval of 5 °C at a constant RH of 40%. The evolution of the reflected spectra is recorded and the envelope evolution calculated from them is illustrated in Fig. 8(a) and (b). The spectra exhibit a red shift during the temperature increasing process. The relationship between the dip wavelength and temperature is illustrated in Fig. 8(c). The temperature sensitivity is calculated through linear fitting as 0.381 nm/°C.

Optics EXPRESS

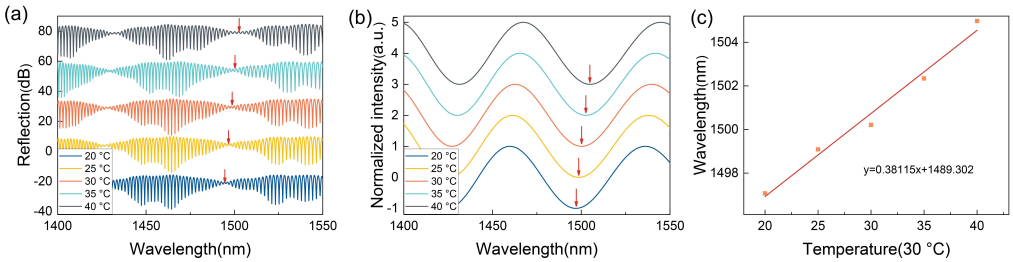

Fig. 8. (a) The reflected spectra evolution during the temperature response experiment; (b) envelopes demodulated using the DSP method; (c) the wavelength at different temperatures and the relevant linear fitting result.

3.4. Response time

The response time of our RH sensor is investigated by using the experimental setup shown in Fig. 9. Probing signal pumped from a tunable laser launched into the sensing system and reflected from the sensing head. The wavelength was fixed at 1535 nm, located in the center of a resonance peak and its adjacent valley in the reflected spectrum, which facilitates higher sensitivity and better monotonicity. The reflected light was received by a photoelectric detector (PD) and recorded via a data acquisition (DAQ) card with a sampling frequency of 100Hz. The sensor was fixed on an electric displacement platform which can vertically adjust the position of the sensing probe rapidly. A bottle of saturated salt solution was placed under the probe to provide a humidity condition different from that in the air.

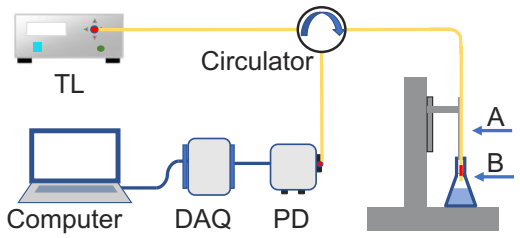

Fig. 9. The experimental setup for response time measurement.

During the experiment, the proposed sensor head was moved downward from position A to position B in about 100 ms by adjusting the displacement stage. Ten minutes later, the sensing probe is raised from position B to A with 100 ms. During the two processes, the relative intensity collected by the PD is shown in Fig. 10. The response times for the sensor at the two processes are 351ms and 455ms, respectively. The fast response of our sensor may be attributed to the compact size and thin film thickness, which means it can realize real-time monitoring of humidity changes related to human breathing and environment monitoring.

3.5. Multi-point RH sensing

Three samples were fabricated to further demonstrate the multi-point RH sensing capability of our sensor combined with the proposed DSP method. The samples are labeled as 1, 2 and 3 with HCBF length as 423 μm, 552 μm and 671 μm, respectively. The independent reflected spectra of the three samples are shown in Fig. 12(a), (b) and (c). The corresponding spatial frequency spectra are shown in Fig. 12(e). To distinguish the reflected signals from the three samples, their HCBF lengths were well designed. The peaks in the three FFT spectra used to extract sensing

Optics EXPRESS

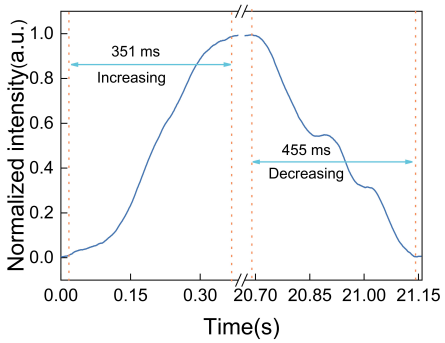

Fig. 10. Response time of the sensor to relative humidity.

signals and calculate envelopes do not overlap with each other. Then, the three sensors were connected to a coupler in parallel, as shown in Fig. 11. The signal light launched from the BBS will be split and coupled into the three samples. The reflected signals passed through the coupler are recorded by the OSA and processed by the computer connected to the OSA. The superimposed interference spectrum with complex fluctuation is observed (see in Fig. 12(d)). The excessively complicated interference fringes make it difficult to obtain valuable RH information of each sensor from the wavelength domain. Therefore, our DSP were conducted to analyze the superimposed spectrum, and the result of the FFT spectrum are shown in Fig. 12(f). Comparing Fig. 12(e) and (f), we can find that the normalized amplitudes of the peaks in the superimposed FFT spectrum are much smaller than the values of peaks in Fig. 12(e). However, the related abscissa positions and shapes of the three pairs of peaks from the superimposed spectra are the same as those from the independent reflected spectra. This is consistent with our theoretical expectations. The three groups of peaks were extracted from the superimposed FFT spectrum by using three bandpass filters. Then, the envelopes are calculated from the three peaks using our DSP method, as shown in Fig. 12(a), (b) and (c)(black lines). It is obvious that the three curves demodulated from the superimposed spectrum match well with the independent reflected spectra of the three samples. It means our DSP method can figure out the Vernier effect-related envelope effectively and accurately based on the superimposed complex spectrum. Therefore, the RH sensing signals from each of the three sensors can be demodulated individually to realize multi-point RH sensing.

Fig. 11. The experimental setup for multi-point relative humidity measurement.

To demonstrate the multi-point sensing capability, samples 1 and 3 were placed at room temperature (27 °C) and 48% RH, while sample 2 was mounted inside the humidity chamber. The humidity changed in the same way as described in the previous section. The schematic diagram of the RH conditions where the samples are placed with time is shown in Fig. 13(d). The DSP was carried out, and the envelopes related to each sample were extracted from the reflected

Optics EXPRESS

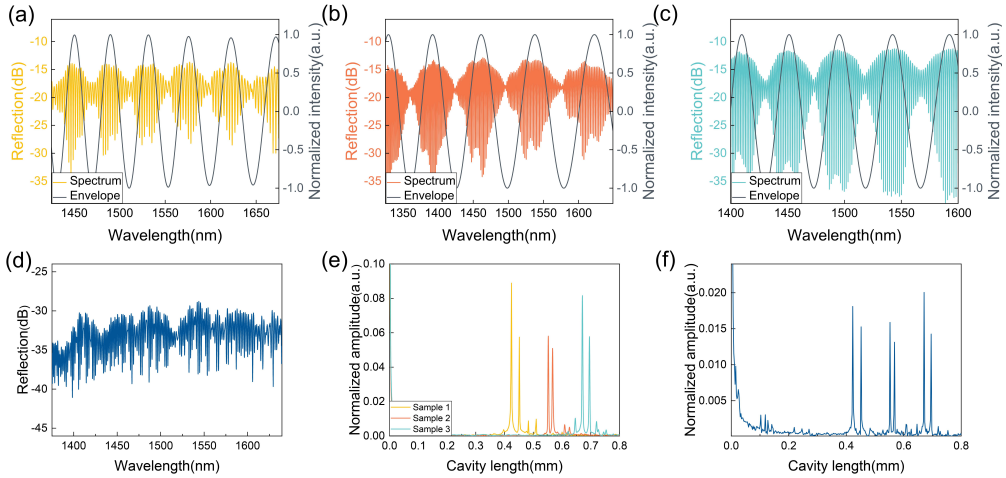

Fig. 12. The independent reflected spectra of the three samples and the three envelopes demodulated from the superimposed spectra: (a) sample 1, (b) sample 2, and (c) sample 3. (d) The superimposed interference spectrum reflected from the three samples. (e) The independent FFT spectra corresponding to the three samples. (f) The FFT spectra corresponding to the superimposed spectrum.

interference spectra and illustrated in Fig. 13(a), (b) and (c), respectively. The dip wavelength around 1500 nm at 45% RH was chosen as the original tracing wavelength to analyze the RH sensitivity. As shown in Fig. 13(e), the wavelength redshifts with time for sample 2, while those for sample 1 and sample 3 keep almost unchanged during this process because the two sensing probes are fixed in a constant temperature and RH environment. The wavelength as a function of RH values for sample 2 is shown in Fig. 13(f). The RH sensitivity measured here is 1.45 nm/% RH, which is consistent with the previously obtained value of 1.42 nm/% RH.

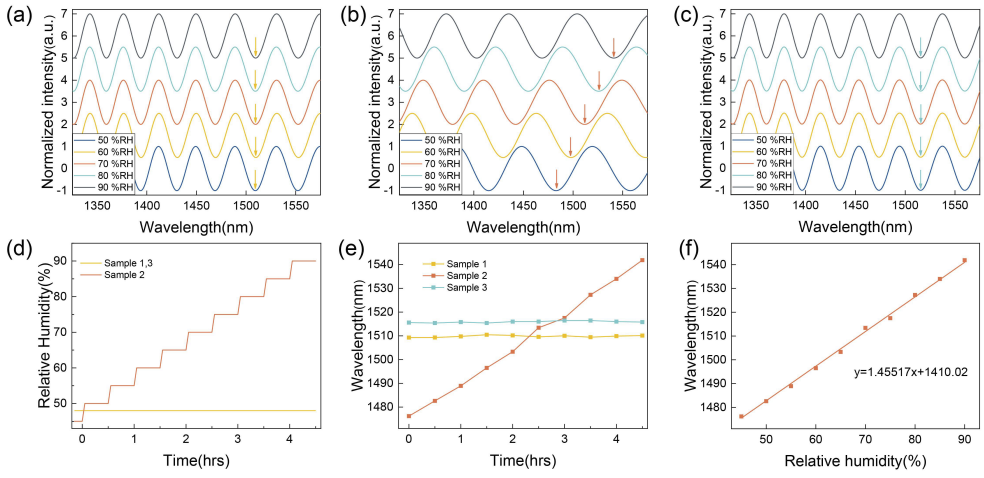

Fig. 13. (a)-(c) The reflected envelopes evolution during the multi-point relative humidity response experiment. (d) The schematic diagram of the RH conditions where the samples are placed with time. (e) Variation of wavelengths with time. (f) The wavelengths at different RH and the relevant linear fitting result.

Optics EXPRESS

3.6. Discussion

Several optical fiber RH sensors based on various principles are listed in table 1. Thanks to the thin chitosan/UVOA film and the Vernier effect generated by the triple-beam interferometer, our sensor has higher sensitivity than other works. At the same time, our DSP algorithm contributes to accurately extracting valuable sensing signals from the complex reflection spectrum and renders our sensing system multi-point sensing capability. Note that the composite film is thicker than the pure chitosan film proposed in other works [17,30], which is not conducive to further improving RH sensitivity. However, the fringe and envelope visibilities of our sensors are much higher. Meanwhile, the film cured by UV exposure has higher mechanical strength and stability. Therefore, our proposed sensor fabrication processes are an optimized tradeoff between theoretical sensitivity and practicability.

Table 1. Comparison of various optical fiber humidity sensors performance

Types	Material	Sensitivity	Range	Multi-point measurement
MZI [39]	ZnO	0.0205 nm/%RH	35%-60%	N
MZI [40]	PVA	0.186 nm/%RH	30%-95%	N
MKR [41]	PVA	0.870 nm/%RH	20%-80%	N
SI [42]	PVA	0.422 nm/%RH	30%-90%	N
FPI [17]	chitosan	0.13 nm/%RH	20%-95%	N
FPI [15]	GQDs-PVA	0.117 nm/%RH	13%-81%	N
FPI [This work]	chitosan/UVOA	1.42 nm/%RH	45%-90%	Y

The dynamic range of the sensor is limited by the oscillation period of the spectral envelope. RH values out of this range may lead to ambiguity since adjacent fringes of the envelope will be mistaken. Therefore, the dynamic range DR should be limited by the FSR of the sensor and the RH sensitivity (S_{RH}), which can be expressed as:

$$DR < \frac{FSR}{S_{RH}}. \tag{17}$$

The sensitivity of our sensor can be derived from Eq. (7) as:

$$S_{RH} = \frac{\Delta\lambda_{en}}{\Delta RH} = \frac{\lambda\Delta(dn_2)}{dn_2\Delta RH}. \tag{18}$$

For our sensor, the phase of Vernier-effect related envelope is the same as $cos(2\phi_2)$, i.e., $cos(4\pi n_2 d/\lambda)$. Therefore, the FSR can be derived as [43]:

$$FSR = \frac{\lambda^2}{2dn_2}. \tag{19}$$

Substituting Eq. (18) and Eq. (19) into Eq. (17), giving:

$$DR < \frac{FSR}{S_{RH}} = \frac{\lambda}{2}\left(n_2\frac{\Delta d}{\Delta RH} + d\frac{\Delta n_2}{\Delta RH}\right)^{-1}. \tag{20}$$

Since the film is very thin, we can assume that the RH dependence of RI and film thickness, i.e., $\Delta d/\Delta RH$ and $\Delta n_2/\Delta RH$ are the same in polymer films with different thicknesses. Therefore, according to Eq. (18), Eq. (19) and Eq. (20), with the decrease of the film thickness, all the RH response sensitivity, FSR and dynamic range are increased. For practical applications, the thickness of the polymer film must be carefully optimized to ensure that the DR of the sensor can

Optics EXPRESS

cover the range of RH to be measured while also considering the film's mechanical strength and sensitivity.

In fact, most other FPI-based sensors heavily rely on expensive high-precision equipment to fabricate extremely short cavities to improve sensitivities. However, the sensitivity of our sensor based on the Vernier effect is determined by the thickness and material of the thin film, but not the length of the hollow-core fiber [30]. The length of the HCBF precisely sliced in our sensor can reach hundreds of micrometers or even a few millimeters while maintaining high sensitivity. It not only reduces the difficulty of glass processing but also increases the sensitivity of our multi-point RH sensor. Signals from all sensors can be separated from each other on the FFT spectrum by adjusting the length of the HCBF. Due to the independence of the HCBF length and the RH sensitivity, we can realize multi-point detection by connecting multiple samples with different lengths while ensuring high sensitivity for each sample.

The longer hollow-core fiber length is beneficial for sensor fabrication and multi-point multiplexing; however, it leads to a weaker light reflection from the polymer thin film, resulting in lower fringe visibility. Due to this, it is necessary for the hollow-core fiber used here to support signal light transmission at low loss. Additionally, sufficient periods are essential to ensure the visibility and separation of the two peaks in the FFT spectrum, as too few periods lead to an overlap of the two peaks, resulting in inaccuracy in the envelope retrieval. Therefore, a fiber with a broader transmission window is preferred to enable more periods of fringes in the reflected interference spectrum. According to the above two requirements, we designed, fabricated and used the HCBF. Light is guided in the fiber with low transmission loss thanks to the concentric ring silica layers with high- and low- RI. Meanwhile, the bandwidth of the guided band based on this ARROW effect is broad, reaching 300 nm (from 1350 nm to 1650 nm) in our HCBF. This low-loss broadband transmission property is essential to ensure the quality of the spectra.

Overall, the superior performance of our sensor is derived from the broadband and low-loss light transmission properties of the HCBF, the use of our two-step film fabrication process to build a thin film with high reflectivity and a well-designed DSP algorithm to demodulate the Vernier effect envelope from the complex superimposed spectrum. All three factors are essential to manufacturing our multi-point, high-sensitivity humidity sensing system.

4. Conclusion

In this paper, we designed and fabricated a highly-sensitive RH sensor based on FPIs and the Vernier effect. The sensor is fabricated by splicing an SMF with a section of HCBF, where a hygroscopic thin film composed of chitosan and UVOA is immobilized at its tip. DSP algorithms based on FFT, filtering and IFFT are proposed to demodulate the sensing signal. The feasibility and effectiveness of this method are theoretically analyzed and experimentally demonstrated. High-sensitivity multi-point RH sensing is realized due to the Vernier effect related to our sensing structure, the transmission properties of HCBF and the well-designed DSP algorithm. The proposed sensor exhibits a high sensitivity of 1.45 nm/% RH, ranging from 45% RH to 90% RH. The entire fabrication process is simple, safe and low-cost, making our sensor a promising candidate for RH monitoring. In addition, the proposed DSP algorithms have considerable potentials for other interferometer-based sensors.

Funding. Shenzhen Municipal Science and Technology Innovation Commission project (A0034676); Hong Kong Government Research Grants Council General Research Fund (GRF) under Project PolyU (15224521).

Disclosures. The authors declare no conflicts of interest.

Data availability. No data were generated or analyzed in the presented research.

References

1. Z. Chen and C. Lu, "Humidity sensors: a review of materials and mechanisms," Sens. Lett. **3**(4), 274–295 (2005).
2. C.-Y. Lee and G.-B. Lee, "Humidity sensors: a review," Sens. Lett. **3**(1), 1–15 (2005).

Optics EXPRESS

3. P. Mecenas, R. T. d. R. M. Bastos, A. C. R. Vallinoto, and D. Normando, "Effects of temperature and humidity on the spread of covid-19: A systematic review," PLoS One **15**(9), e0238339 (2020).
4. P. Wolkoff, "Indoor air humidity, air quality, and health–an overview," Int. J. Hyg. Environ. Health **221**(3), 376–390 (2018).
5. Q.-N. Zhao, Y.-J. Zhang, Z.-H. Duan, S. Wang, C. Liu, Y.-D. Jiang, and H.-L. Tai, "A review on ti3c2tx-based nanomaterials: synthesis and applications in gas and humidity sensors," Rare Met. **40**(6), 1459–1476 (2021).
6. M. A. Najeeb, Z. Ahmad, and R. A. Shakoor, "Organic thin-film capacitive and resistive humidity sensors: a focus review," Adv. Mater. Interfaces **5**(21), 1800969 (2018).
7. Y. Peng, Y. Zhao, M.-Q. Chen, and F. Xia, "Research advances in microfiber humidity sensors," Small **14**(29), 1800524 (2018).
8. N. Lazarus, S. S. Bedair, C.-C. Lo, and G. K. Fedder, "Cmos-mems capacitive humidity sensor," J. Microelectromech. Syst. **19**(1), 183–191 (2010).
9. J. Boudaden, M. Steinmaßl, H.-E. Endres, A. Drost, I. Eisele, C. Kutter, and P. Müller-Buschbaum, "Polyimide-based capacitive humidity sensor," Sensors **18**(5), 1516 (2018).
10. J. Ascorbe, J. M. Corres, F. J. Arregui, and I. R. Matias, "Recent developments in fiber optics humidity sensors," Sensors **17**(4), 893 (2017).
11. Y. Wang, G. Yan, Z. Lian, C. Wu, and S. He, "Liquid-level sensing based on a hollow core bragg fiber," Opt. Express **26**(17), 21656–21663 (2018).
12. S. Pevec and D. Donlagić, "Multiparameter fiber-optic sensors: A review," Opt. Eng. **58**(07), 1 (2019).
13. P. Lu, N. Lalam, M. Badar, B. Liu, B. T. Chorpening, M. P. Buric, and P. R. Ohodnicki, "Distributed optical fiber sensing: Review and perspective," Appl. Phys. Rev. **6**(4), 041302 (2019).
14. R. da Silva Marques, A. R. Prado, P. F. da Costa Antunes, P. S. de Brito André, M. Ribeiro, A. Frizera-Neto, and M. J. Pontes, "Corrosion resistant fbg-based quasi-distributed sensor for crude oil tank dynamic temperature profile monitoring," Sensors **15**(12), 30693–30703 (2015).
15. Y. Zhao, R.-j. Tong, M.-Q. Chen, and F. Xia, "Relative humidity sensor based on hollow core fiber filled with gqds-pva," Sens. Actuators, B **284**, 96–102 (2019).
16. J. Mathew, Y. Semenova, and G. Farrell, "Relative humidity sensor based on an agarose-infiltrated photonic crystal fiber interferometer," IEEE J. Sel. Top. Quantum Electron. **18**(5), 1553–1559 (2012).
17. L. H. Chen, T. Li, C. C. Chan, R. Menon, P. Balamurali, M. Shaillender, B. Neu, X. Ang, P. Zu, W. Wong, and K. C. Leong, "Chitosan based fiber-optic fabry–perot humidity sensor," Sens. Actuators, B **169**, 167–172 (2012).
18. J. M. Corres, F. J. Arregui, and I. R. Matias, "Design of humidity sensors based on tapered optical fibers," J. Lightwave Technol. **24**(11), 4329–4336 (2006).
19. J. Ascorbe, J. Corres, I. Matias, and F. Arregui, "High sensitivity humidity sensor based on cladding-etched optical fiber and lossy mode resonances," Sens. Actuators, B **233**, 7–16 (2016).
20. Z. Zhang, H. Gong, C. Yu, K. Ni, and C. Zhao, "An optical fiber humidity sensor based on femtosecond laser micromachining fabry-perot cavity with composite film," Opt. Laser Technol. **150**, 107949 (2022).
21. D. Su, X. Qiao, Q. Rong, H. Sun, J. Zhang, Z. Bai, Y. Du, D. Feng, Y. Wang, M. Hu, and Z. Feng, "A fiber fabry–perot interferometer based on a pva coating for humidity measurement," Opt. Commun. **311**, 107–110 (2013).
22. S. Wu, G. Yan, Z. Lian, X. Chen, B. Zhou, and S. He, "An open-cavity fabry-perot interferometer with pva coating for simultaneous measurement of relative humidity and temperature," Sens. Actuators, B **225**, 50–56 (2016).
23. J. S. Santos, I. M. Raimundo Jr, C. M. Cordeiro, C. R. Biazoli, C. A. Gouveia, and P. A. Jorge, "Characterisation of a nafion film by optical fibre fabry–perot interferometry for humidity sensing," Sens. Actuators, B **196**, 99–105 (2014).
24. C. Huang, W. Xie, M. Yang, J. Dai, and B. Zhang, "Optical fiber fabry–perot humidity sensor based on porous al 2 o 3 film," IEEE Photonics Technol. Lett. **27**(20), 2127–2130 (2015).
25. C. Lang, Y. Liu, J. Ye, M. Chen, Y. Li, and S. Qu, "An ultra-sensitive fiber sensor for micro-newton contact force detection based on a polymerized hollow-cylinder by one-step fabrication," IEEE Sens. J. **21**(22), 25710–25715 (2021).
26. M.-q. Chen, Y. Zhao, H.-m Wei, C.-l Zhu, and S. Krishnaswamy, "3d printed castle style fabry-perot microcavity on optical fiber tip as a highly sensitive humidity sensor," Sens. Actuators, B **328**, 128981 (2021).
27. Y. Liu, X. Li, Y.-n. Zhang, and Y. Zhao, "Fiber-optic sensors based on vernier effect," Measurement **167**, 108451 (2021).
28. A. D. Gomes, H. Bartelt, and O. Fraz ao, "Optical vernier effect: recent advances and developments," Laser Photonics Rev. **15**(7), 2000588 (2021).
29. Y. Chen, L. Zhao, S. Hao, and J. Tang, "Advanced fiber sensors based on the vernier effect," Sensors **22**(7), 2694 (2022).
30. C. Zhou, Q. Zhou, B. Wang, J. Tian, and Y. Yao, "High-sensitivity relative humidity fiber-optic sensor based on an internal–external fabry–perot cavity vernier effect," Opt. Express **29**(8), 11854–11868 (2021).
31. N. Litchinitser, A. Abeeluck, C. Headley, and B. Eggleton, "Antiresonant reflecting photonic crystal optical waveguides," Opt. Lett. **27**(18), 1592–1594 (2002).
32. H. Su and X. G. Huang, "Fresnel-reflection-based fiber sensor for on-line measurement of solute concentration in solutions," Sens. Actuators, B **126**(2), 579–582 (2007).
33. W.-H. Tsai and C.-J. Lin, "A novel structure for the intrinsic fabry-perot fiber-optic temperature sensor," J. Lightwave Technol. **19**(5), 682–686 (2001).

Optics EXPRESS

34. P. Zhang, M. Tang, F. Gao, B. Zhu, Z. Zhao, L. Duan, S. Fu, J. Ouyang, H. Wei, P. P. Shum, and D. Liu, "Simplified hollow-core fiber-based fabry–perot interferometer with modified vernier effect for highly sensitive high-temperature measurement," IEEE Photonics J. **7**(1), 1–10 (2015).
35. Y. Jiang, "Fourier transform white-light interferometry for the measurement of fiber-optic extrinsic fabry–perot interferometric sensors," IEEE Photonics Technol. Lett. **20**(2), 75–77 (2008).
36. Y. Jiang and C. Tang, "Fourier transform white-light interferometry based spatial frequency-division multiplexing of extrinsic fabry–pérot interferometric sensors," Rev. Sci. Instrum. **79**(10), 106105 (2008).
37. Q. Yu and X. Zhou, "Pressure sensor based on the fiber-optic extrinsic fabry-perot interferometer," Photonic Sens. **1**(1), 72–83 (2011).
38. A. Al Noman, J. N. Dash, X. Cheng, C. Y. Leong, H.-Y. Tam, and C. Yu, "Hydrogel based fabry-pérot cavity for a ph sensor," Opt. Express **28**(26), 39640–39648 (2020).
39. A. Lokman, H. Arof, S. W. Harun, Z. Harith, H. A. Rafaie, and R. M. Nor, "Optical fiber relative humidity sensor based on inline mach–zehnder interferometer with zno nanowires coating," IEEE Sens. J. **16**(2), 312–316 (2016).
40. Y. Zhao, Y. Peng, M.-q. Chen, and R.-J. Tong, "Humidity sensor based on unsymmetrical u-shaped microfiber with a polyvinyl alcohol overlay," Sens. Actuators, B **263**, 312–318 (2018).
41. J. C. Shin, M.-S. Yoon, and Y.-G. Han, "Relative humidity sensor based on an optical microfiber knot resonator with a polyvinyl alcohol overlay," J. Lightwave Technol. **34**(19), 4511–4515 (2016).
42. L.-P. Sun, J. Li, L. Jin, Y. Ran, and B.-O. Guan, "High-birefringence microfiber sagnac interferometer based humidity sensor," Sens. Actuators, B **231**, 696–700 (2016).
43. Z. Li, Y. Zhang, C. Ren, Z. Sui, and J. Li, "A high sensitivity temperature sensing probe based on microfiber fabry-perot interference," Sensors **19**(8), 1819 (2019).